Supplementary Information

Luminescent Coordination Polymers for the VIS and NIR Range Constituting from LnCl₃ and 1,2-bis(4-pyridyl)-ethane

N. Dannenbauer,[a] P. R. Matthes[a] and K. Müller-Buschbaum[a]

[a] Institut für Anorganische Chemie, Julius-Maximilians-Universität, Am Hubland, 97074 Würzburg, Germany, E-mail: k.mueller-buschaum@uni-wuerzburg.de; Fax: (+)49-931-3184785; Tel: (+)49-931-3188724
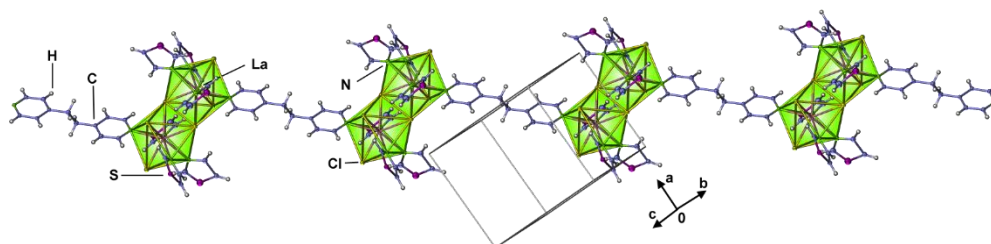
Figure S1. Depiction of the one-dimensional strand of $^1_\infty$[La$_2$Cl$_6$(bpe)$_2$(thz)$_6$](1) showing bpe linkage of La$_2$Cl$_6$ dimers. Thermal ellipsoids depict 50 % of the probability level of the atoms.
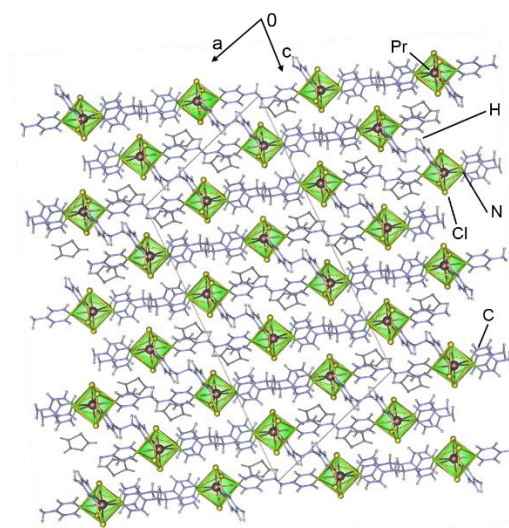

Figure S2. View along the b-axis of the crystal structure of $^3_\infty$[PrCl$_3$(bpe)$_2$]·thz(3). Intercalated thiazole molecules are illustrated in grey.
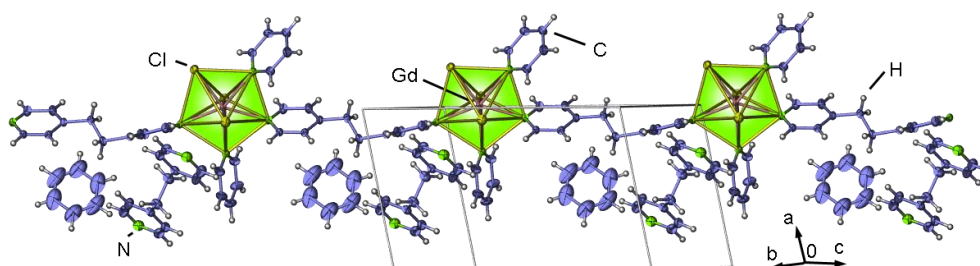
Figure S3. Depiction of the one-dimensional strand of $^1_\infty$[GdCl$_3$(bpe)(py)$_2$]·(bpe/py) (13). Thermal ellipsoids depict 50 % of the probability level of the atoms. The intercalated pyridine molecule is described with a benzene molecule, due to rotational disorder effects.

Figure S4. Depiction of the crystal structure of $\frac{1}{\infty}$[GdCl₃(bpe)(py)₂]·(bpe/py) (**13**) along *c*-axis. Thermal ellipsoids depict 50 % of the probability level of the atoms. The intercalated pyridine molecule is described with a benzene molecule, due to rotational disorder effects.
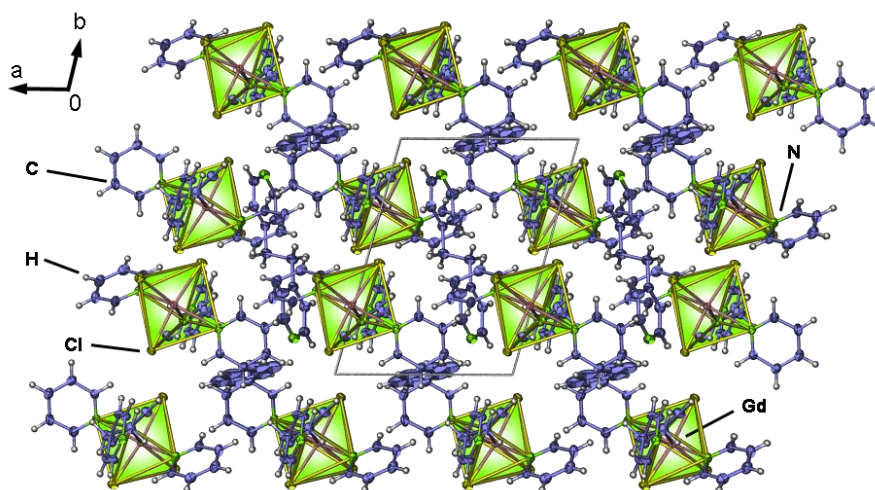
Table S1 : Selected interatomic distances and angles for **1**, **2**, **8**, **11** and **13-14**.

|	La (1)	Ce (2)	Pr (3)	Dy (8)	Yb (11)	Gd (13)	Er (14)
Ln(1)-Cl(1)	2.8212(11)	2.7444(7)	2.7206(7)	2.6332(9)	2.5928(12)	2.6330(12)	2.5822(7)
Ln(1)-Cl(2)	2.8685(9)	2.7415(7)	2.7142(7)	2.6005(11)	2.6002(13)	2.6477(12)	2.5981(7)
Ln(1)-Cl(3)	2.8221(10)	2.7373(7)	2.7127(7)	2.6309(11)	2.5609(13)	2.6864(13)	2.6460(7)
Ln(1)-Cl(2)'	2.9263(11)						
Ln(1)-N(1)	2.728(2)	2.670(2)	2.643(2)	2.522(3)	2.475(4)	2.594(2)	2.546(2)
Ln(1)-N(2)	2.816(2)	2.693(2)	6.670(2)	2.553(3)	2.509(3)		
Ln(1)-N(2)'						2.542(2)	2.492(2)
Ln(1)-N(3)	2.710(2)	2.683(2)	2.661(2)	2.571(4)	2.526(4)	2.570(3)	2.520(2)
Ln(1)-N(4)	2.742(2)	2.653(2)	2.630(2)	2.524(3)	2.473(3)		
(C-C) range	1.510(3)-	1.508(3)-	1.507(4)-	1.507(5)-	1.509(5)-	1.502(6)-	1.502(4)-
	1.537(5)	1.533(3)	1.531(4)	1.54(2)	1.548(8)	1.523(9)	1.520(7)
(C=C, C=N, C=S)	1.311(3)-	1.332(3)-	1.296(4)-	1.257(14)-	1.323(7)-	1.329(6)-	1.325(9)-
range	1.719(3)	1.715(3)	1.708(3)	1.877(7)	1.832(11)	1.395(6)	1.399(4)
Cl(1)-Ln(1)-Cl(2)	87.32(15)	92.25(2)	92.20(2)	89.70(3)	89.73(4)	171.43(3)	172.98(2)
Cl(1)-Ln(1)-Cl(3)	110.76(2)	170.13(2)	170.57(2)	174.32(4)	174.85(4)	91.13(4)	90.60(3)
Cl(2)-Ln(1)-Cl(3)	140.45(2)	93.94(2)	93.65(2)	95.53(4)	95.05(4)	97.10(4)	96.42(2)
N(1)-Ln(1)-Cl(2)	74.43(4)	79.24(4)	79.08(6)	76.42(8)	76.09(9)		
N(1)-Ln(1)-Cl(1)	75.70(4)	84.29(5)	84.47(7)	89.80(10)	89.73(11)		
N(1)-Ln(1)-N(4)	123.08(5)	155.40(6)	155.18(8)	152.28(12)	151.40(13)	70.05(10)	70.03(8)
N(1)-Ln(1)-N(2)	79.42(5)	67.41(5)	67.43(7)	67.94(10)	68.24(12)		
N(2)-Ln(1)-N(3)	67.55(5)	70.67(5)	70.76(7)	72.24(10)	72.06(11)		
N(3)-Ln(1)-N(4)	75.06(5)	68.62(5)	68.77(7)	67.92(12)	68.59(12)		
N(1)-Ln(1)-N(3)	144.35(5)	133.48(5)	133.63(7)	139.74(10)	139.93(12)	67.59(10)	68.10(8)
Cl(3)-Ln(1)-N(1)	76.40(4)	104.42(5)	103.90(7)	93.59(10)	93.28(11)		
Cl(2)-Ln(1)-N(2)	74.39(4)	143.82(4)	143.70(5)	144.36(7)	144.33(8)		
Cl(1)-Ln(1)-N(2)	152.08(4)	97.82(4)	97.91(6)	90.17(7)	90.03(9)		
Cl(3)-Ln(1)-N(2)	74.24(4)	81.63(4)	81.64(6)	86.88(8)	87.21(9)		
N(4)-Ln(1)-Cl(3)	72.51(4)	84.35(4)	84.64(5)	87.01(10)	87.82(11)		
N(2)'-Ln(1)-N(4)						71.13(10)	71.09(7)
Cl(3)-Ln(1)-N(3)						75.25(8)	75.05(6)
Cl(3)-Ln(1)-N(2)'						76.36(8)	76.12(6)
N(2)'-Ln(1)-N(1)						140.73(10)	140.66(8)

Symmetry operation : [I] +x, +y, -1+z
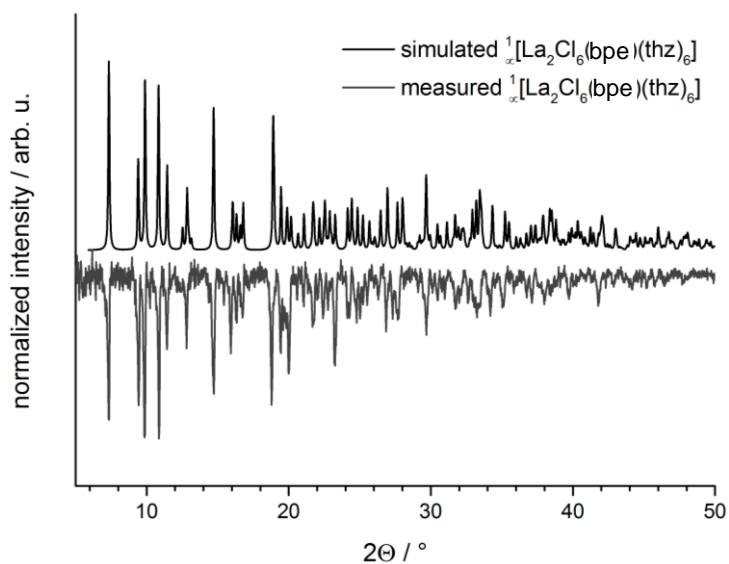
Figure S5. Comparison of the simulated diffraction pattern (top) of the single-crystal X-ray structure determination of $^1_\infty$[La$_2$Cl$_6$(bpe)(thz)$_6$](**1**) at 100 K with the observed powder X-ray diffraction patterns (Cu-radiation) at RT (bottom).
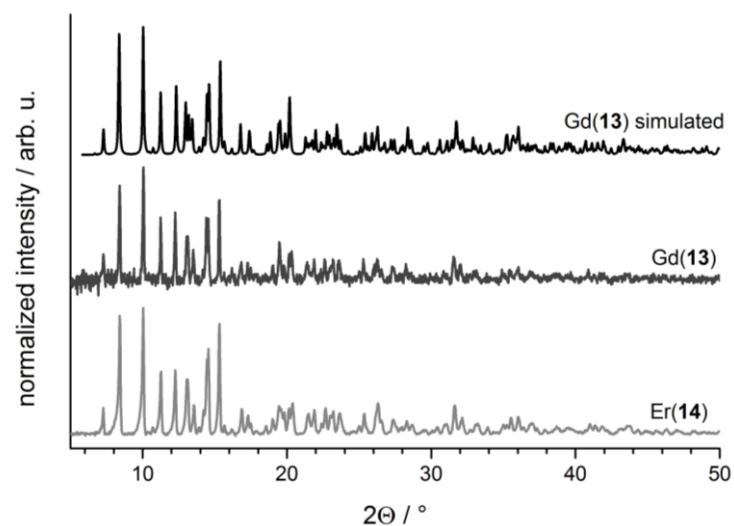
Figure S6. Comparison of the observed powder X-ray diffraction patterns (Cu-radiation) of isotypic $^1_\infty$[LnCl$_3$(bpe)(py)$_2$]·(bpe/py) with Ln = Gd(**13**), Er(**14**) with the simulated diffraction pattern of the single-crystal X-ray structure determination of **13**(Gd) at 168K.
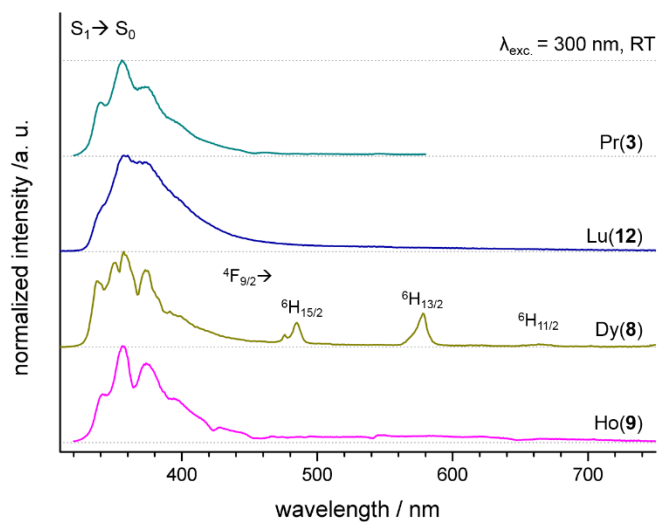
Figure S7. Solid state emission spectra of the compounds $^3_\infty$[LnCl$_3$(bpe)$_2$]·thz (**3, 8, 9** and **12**) at RT.
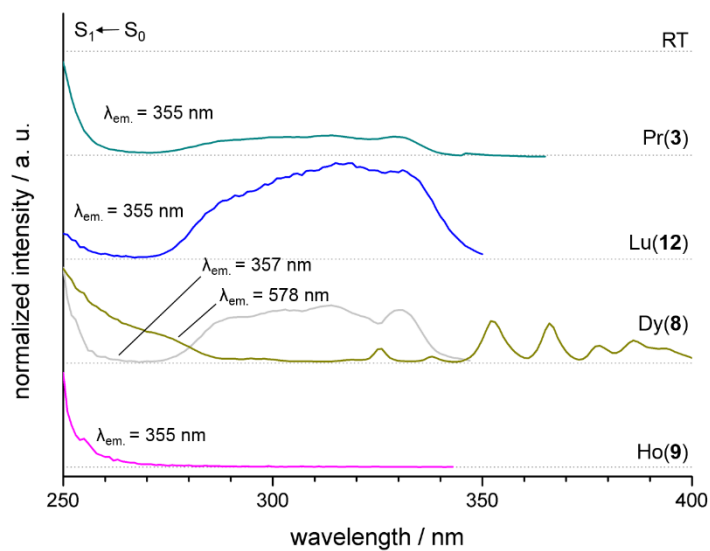
Figure S8. Solid state excitation spectra of the compounds $^3_\infty[LnCl_3(bpe)_2]\cdot thz$ (**3, 8, 9** and **12**) at RT.
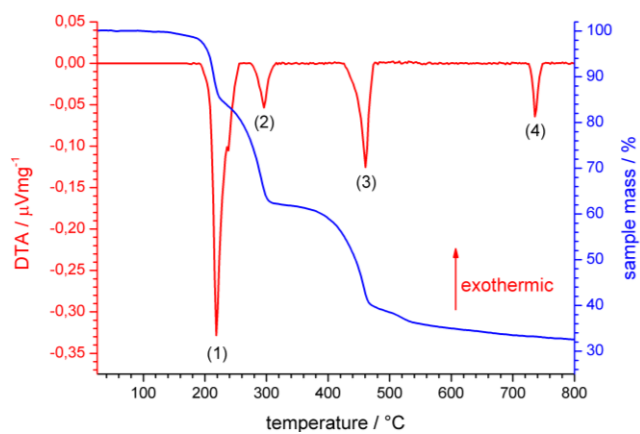
Figure S9. DTA/TG investigation of $^3_\infty[NdCl_3(bpe)_2]\cdot thz$ (**4**) performed with a heating rate of 10°C/min and a flow rate of 20 ml min^{-1} Ar and 20 ml N$_2$ min^{-1}.
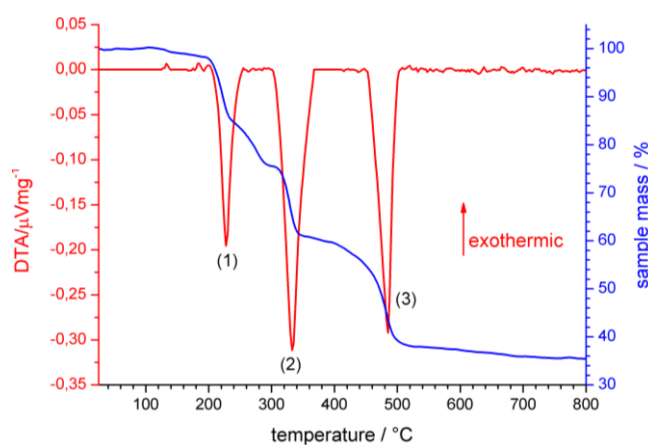
Figure S10. DTA/TG investigation of $^3_\infty[GdCl_3(bpe)_2]\cdot thz$ (**6**) performed with a heating rate of 10°C/min and a flow rate of 20 ml min^{-1} Ar and 20 ml N$_2$ min^{-1}.
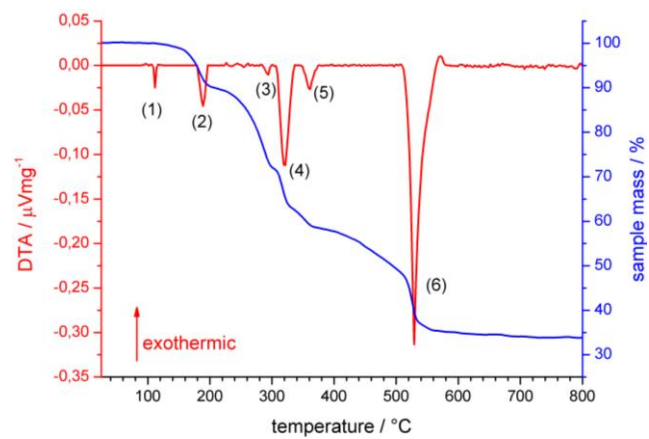
Figure S11. DTA/TG investigation of $^3_\infty$[YbCl$_3$(bpe)$_2$]·thz (**11**) performed with a heating rate of 10°C/min and a flow rate of 20 ml min^{-1} Ar and 20 ml N$_2$ min^{-1}.